Real-Time Temperature Monitoring for Mechanical Oscillators

California Institute of Technology
LIGO Summer Undergraduate Research Fellowship

Mandy Katherine Cheung[a], Aaron Markowitz[b], Brittany Kamai[b], Rana X. Adhikari[b]

[a] *Pasadena City College, Pasadena, CA 91106*
[b] *LIGO Laboratory, California Institute of Technology, Pasadena, CA 91125*

Abstract

Approaching the next generation of Laser Interferometer Gravitational-Wave Observatory (LIGO) detectors, namely LIGO Voyager, there are planned improvements to the ITM/ETM components of the core optics. It is theorized that utilizing coated silicon test masses, cryogenically cooled to 123 K, will drastically reduce thermal noise due to the assumption that the material's CTE reaches a zero-crossing point at around this temperature. CryoQ is the experimental setup intended to characterize possible coating types for these optics. Temperature monitoring and control is an important consideration of this procedure. This summer research project aims to contribute to a method of temperature monitoring that is direct while not making any physical contact with the silicon sample. Making use of data that CryoQ already collects, the project exploits the temperature dependency of a material's eigenmodes. Tracking shifts in the corresponding eigenfrequencies to shifts in temperature allows for a reliable way to obtain real-time temperature monitoring of the coated silicon samples. Following preparation in which RTDs are implemented and modal data is collected, the calibration is calculated and the method's feasibility is confirmed. Future steps require further data collection and a modified control loop to be applied to the system.

Keywords:
LIGO, gravitational waves, CryoQ, temperature monitoring, eignfreqency, eigenmode

1. Introduction

Manifested by over a century's worth of innovative thinking and collaborative effort, the Laser Interferometer Gravitational-wave Observatory (LIGO) satisfies a fundamental desire to illuminate more of the universe than ever before. The foundation of this project truly begins with the 1916 publication of Albert Einstein's paper "On the Theory of General Relativity," in which he solidifies a basis for the concept of gravitational radiation [1].

Email address: mandykatche@gmail.com (Mandy Katherine Cheung)

[1] Some consider "Sur la dynamique d' l'électron," written by Henri Poincaré in 1905, as the earliest mention of gravitational waves [1, 2].

As a result of the linearized weak-field approximations put forth by Einstein's general relativity theory, gravitational waves are defined as radiating distortions to the curvature of space-time caused by accelerating masses [3, 4]. It would prove to be a challenging course in reaching conclusive evidence for the existence of gravitational waves, and even more so, their detection. Growing development in the field of gravitational physics required the contribution of many. Such milestones would perhaps include the gravitational redshift experiment [2] , the discovery of the Hulse-Taylor binary [3] , and the discovery of the Twin Quasar as a gravitational lens [4] . By the turn of the century, making its mark as the primary method of practically detecting and measuring gravitational waves, LIGO is officially implemented. However, it would not be until another decade and a half before design improvements could be made, allowing for a proper detection. Merely days after the upgrade to Advanced LIGO (aLIGO), on September 14th, 2015, the world got its first direct "glimpse" of a gravitational wave [8]. It had resulted from the collision of two black holes, 1.3 billion light years away.

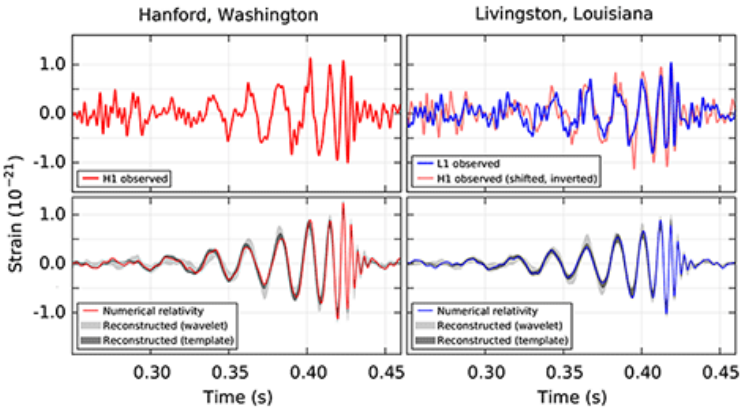

Figure 1: The first detection, GW091415, data collected from both LIGO sites (Hanford and Livingston), in comparison with one another, and in comparison with the numerical relativity models, graphed as detector strain versus time. [8].

[2]In 1959, Robert Pound and Glen A. Rebka Jr performed the first gravitational redshift test, the Pound-Rebka experiment. [5]

[3]In 1974, Russell Hulse and Joseph Taylor were the first to discover a binary pulsar. It was apparent that this would be an incredible opportunity to test Einstein's theory of general relativity.[6]

[4]In 1979, Dennis Walsh, Robert Carswell and Ray Weyman discovered the first gravitational lens. QSO 0957+561, the Twin Quasar, appeared as two images and offered further insight into Einstein's prediction of the effect of mass bending light [7]

1.1. The Detectors

LIGO, analogous to a pair of ears, currently operates two detectors. Both detectors are based in America, the first is located in Hanford, Washington and the second is located in Livingston, Louisiana. Separated by a distance of approximately 3001.8 km, dual detectors are necessary for general localization and as a validation method to account for the noise sources distinct to each site [9]. Furthermore, LIGO is a part of the larger LIGO Scientific Collaboration (LSC, LSC-Virgo). The LSC is a vast world-wide network that unites several interferometric gravitational wave detectors of other institutions, such as KAGRA located in Japan; Virgo located in Italy; and GEO located in Germany.

The LIGO detectors are precision measurement instruments originating from the fundamental concepts of a Michelson interferometer, which is an apparatus capable of measuring wavelength displacements through interference patterns created by the superposition of two light waves. For the essential configuration of a Michelson interferometer, a laser beam is divided through a beam-splitter, resulting in two beams that are sent down separate paths. At the end of each path, the component beam is reflected back towards the center where they meet up with one another. The interferometer can be structured such that the paths are of equal lengths and orthogonal, therefore the beams negate each other when rejoining and produce a destructive interference. It would then be apparent if any slight disturbances occur, as the beams will result in a constructive interference instead.

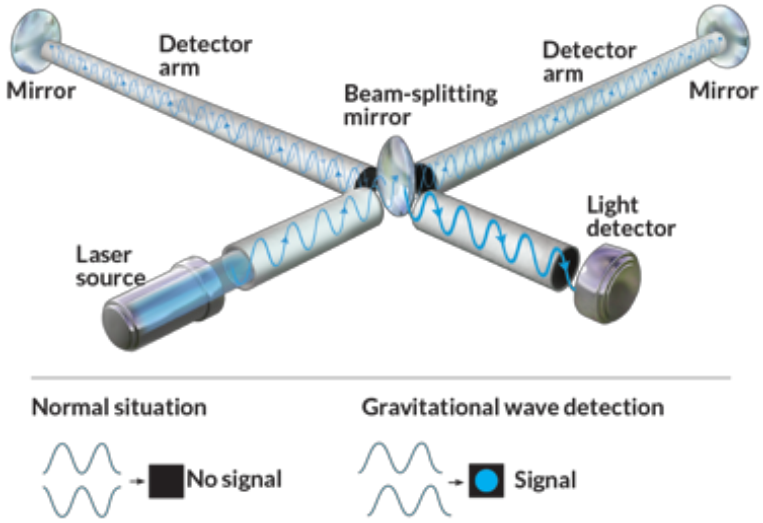

Figure 2: A simplified layout of the LIGO detector, demonstrates constructive and destructive interference as seen by the photodetector [10].

In a similar fashion, the essential configuration of a LIGO detector consists of sending a laser beam through a beam-splitter, then into two orthogonal arms housing the paths of the component beams in vacuum (see Figure 2). However, in order to increase the instrument's sensitivity, the LIGO detector is of a much larger scale and heavily modified. The arms

are 4 kilometers in length each, considerably bigger than a typical Michelson interferometer. Furthermore, one example of a modification utilized by the detector is the addition of a Fabry-Pérot cavity, an optical resonator, in each arm. In LIGO's system, the Fabry-Pérot cavity utilizes an input test mass in addition to the end test mass of an arm to circulate the laser beam continuously with a finesse of approximately 280 [11]. In doing so, the 4 km long arms of the LIGO detector can effectively function as if they were 1,128 km. By prolonging the duration in which a particle might potentially interact with the gravitational wave, there is an increase in sensitivity to the wave's effects. The LIGO detector makes measurements by observing how each arm compresses and stretches in response to a passing gravitational wave. Thus, relating the gravitational-wave strain to displacement in the length of the detector arms.

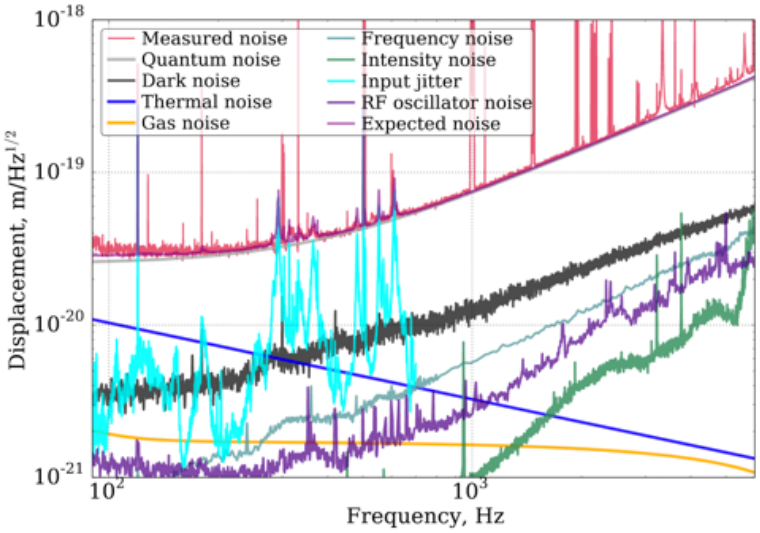

Figure 3: The noise budget plot for the LIGO Hanford instrument at a frequency range between 100 to 1000 Hz. The noise budget is graphed in terms of power spectral density (PSD). Each curve represents a noise term and its power at that frequency [12].

1.2. Strain Sensitivity

As previously emphasized, it is crucial to achieve a certain level of sensitivity. Gravitational waves have extremely small amplitudes. In order for LIGO to detect gravitational-wave strain, the detector must be able to sense displacements smaller than $\frac{1}{10{,}000}th$ of a proton. The most recent generation of detectors, aLIGO, is designed to be capable of perceiving strain fluctuations around an average of $10^{-23}\frac{1}{\sqrt{Hz}}$, between the frequency range of 100 and 1,000 Hz [12]. Unfortunately, with increased sensitivity, it also follows that the instrument is more likely to be disturbed by irrelevant sources of input, or noise. A detector's level of sensitivity is meaningless if it is marred by a large amount of noise. Consequently, it can be said that an instrument's detection threshold is defined by the highest contributing noise level. Lowering the noise floor, the sum of unwanted signals, is vital to improving sensitivity.

The noise budget of LIGO is comprised of many noise terms, such as seismic noise caused by motion from earthquakes or traffic; or gas noise caused by the effects of residual gas particles present in the detector. However, the fundamental sources contributing to LIGO's noise floor are quantum and thermal(see Figure 3) [11]. Quantum noise in the interferometer refers to shot and radiation pressure noises. Shot noise is an issue related to fluctuations in photon arrival rate during detection; and radiation pressure noise is due to random motion in the detector's mirrors caused by radiation from the laser beam. Thermal noise in the interferometer is categorized between the suspension type and the test mass type. Suspension thermal noise can mostly be explained by mechanical loss due to the material of the fibers suspending the test masses. Test mass thermal noise also has several components to differentiate between, but the main concern is coating thermal noise. Coating thermal noise is a result of thermal dissipation in the material of the dielectric coating. These noise terms are the limiting factor in how sensitive the laser interferometer can be.

1.3. LIGO Voyager

With gravitational waves waiting to tell us so much more, the improved precision of the interferometric detector is a never-ending goal. Sensitivity can be increased by addressing the noise terms of the detector, with quantum noise and thermal noise being the most problematic. Planned for official completion in a decade, LIGO Voyager is the next generation of LIGO detectors. LIGO Voyager proposes to handle the issue of thermal noise by operating at a lower temperature. For this purpose, LIGO Voyager will replace the existing fused silica test masses with 200 kg mono-crystalline silicon test masses, and these mirrors will be maintained at a cryogenic temperature of 123 K [13]. Silicon is a suitable choice, because while fused silica does not perform well as an optical material under cryogenic temperatures, silicon's coefficient of thermal expansion approaches a zero-crossing at a temperature range around 123 K [13]. This property will help reduce thermal noise by minimizing thermo-elastic distortions in the mirror. However, to ensure the effectiveness of the test mass change, the substrate coupled with the highly-reflective coating needs to be characterized to determine minimal coating thermal noise. The in-house Caltech experiment, CryoQ, is currently collecting quality factor measurements to determine the best coating type and application method to use.

2. Method

My summer fellowship was work done in support of the CryoQ experiment. Considering that CryoQ makes measurements dependent on a specified temperature of the sample, it is necessary for the setup to have a stable temperature monitoring and control system. It is required for this system to acquire a direct temperature measurement of the sample disk. The issue arises, however, with the other crucial demand of the experiment. Since the measurements made are of the sample's vibrational response to an excitation, any temperature probes in contact with the disk during its ring-down will contribute to mechanical loss and result in an inaccurate measurement of quality factor.

Therefore, my project focused on testing the feasibility of a real-time temperature monitoring system that required minimal physical interaction with the disk. The method makes use of measurements already monitored by the experiment (see Section 2.1), and relies on the temperature dependency of an object's mechanical modes. By tracking both the shift in temperature and the resulting shift in resonant frequency, we can create a calibration curve that will allow us to predict temperature by relying on the monitored resonant frequency.

We must provide two terms, temperature and resonant frequency. CryoQ has already implemented RTDs into its setup as the primary means of collecting temperature data (see Section 2.2). This summer begins with preparing the RTDs for use, this involves a calibration process and testing to ensure proper readout. Then we will move onto getting the physical set up of the CryoQ prepared for Q factor measurements by aligning the beam (see Section 2.3). Following that, we will use the CryoQ experiment to search for and monitor resonant frequencies (see Section 2.4). Once we are able to collect information on temperature and resonant frequencies, we can begin collecting data points for the calibration by manipulating the temperature of the disk and tracking the corresponding shifts.

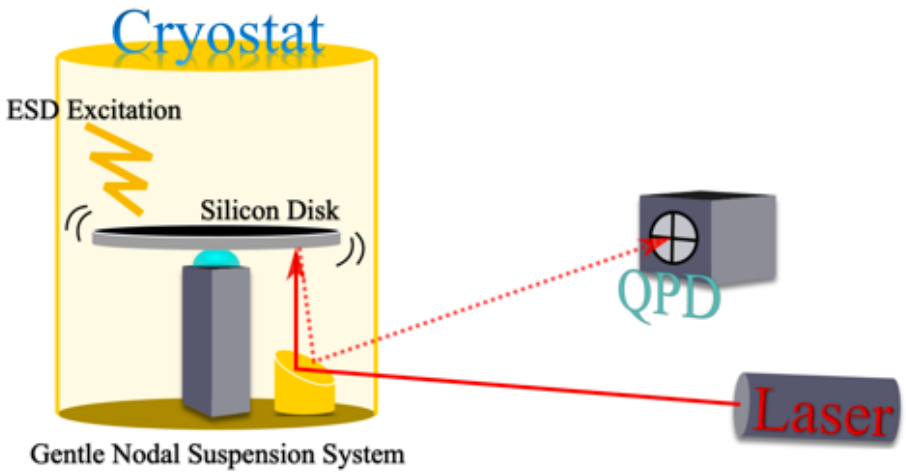

Figure 4: A simplified diagram demonstrating the basic components of the CryoQ experiment configuration. The disk is enclosed in a cryostat where an excitation is sent to the disk through an electrostatic drive (ESD). The disk's response is measured using a laser and quadrant photodiode (QPD) pathway.

2.1. CryoQ

CryoQ, as mentioned, is an experiment designed to optimize the thermal noise reduction efforts for the third-generation detector upgrade by testing suitable optical coatings. For a coating to qualify, it must have low mechanical loss when coupled with the silicon substrate. To determine this, CryoQ measures quality factor. Quality factor is applicable in the analysis of loss for many systems, but essentially it is a way to describe a ratio of energy loss to energy stored in the system. Having a high quality factor translates to being well isolated from

the environment. CryoQ measures the quality factor of several sample disks of silicon with different coatings. The disks are positioned using the Gentle Nodal Suspension system, and housed in a cryostat where the disk can be cooled to 123 K. Once the disk has been cooled, the first thing to do is excite the disk, the experiment uses an electrostatic drive to do so. A laser is then reflected off the disk into a quadrant photodiode, where we can collect data about the disk's pitch and yaw, or motion in the horizontal and vertical axes (see Figure 4).

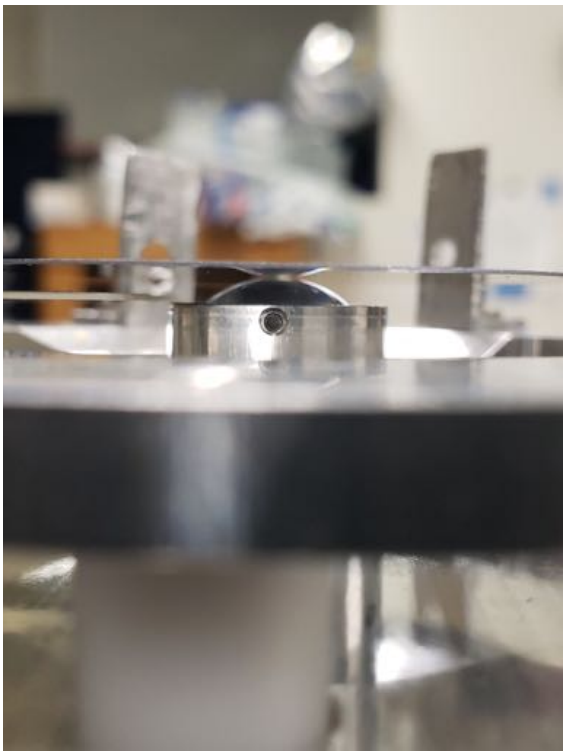

Figure 5: A close-up of GeNS, a specialized suspension system to reduce disturbances created by mechanical clamping. The sample rests on the lens of the system with minimal contact.

To better measurement accuracy, CryoQ utilizes the Gentle Nodal Suspension (GeNS) system (see Figure 5). This system was created as an effort to reduce damping effects caused by mechanical clamping [14]. Traditional suspension methods often require the sample to be fastened to, or perched upon, a structure of some kind. Unfortunately, such an approach allows for the introduction of additional parameters that would increase the difficulty of obtaining Q measurements. GeNS attempts to minimize this issue by minimizing the impact of the suspension structure on the disk. GeNS is composed of an outer and inner frame, the outer frame moves over the inner frame vertically. The outer frame is the substrate holder and accommodates the substrate, or disk, in a specially-sized receptacle. The inner frame has a small post with a lens in the center. First, the disk is placed in the substrate holder, then as this outer frame gets lowered over the inner frame, the substrate holder supporting the disk is lowered past the lens, leaving the disk centered and balanced on the lens.

2.2. Resistance Temperature Detectors

At the beginning of our work this summer, we focused on fulfilling the temperature component of the calibration. A resistance temperature detector (RTD) is a reliable tool used for precision thermometry. RTDs are preferable for their high accuracy. The calibration curve they offer is linear, stable, and reproducible [15]. There are many types of RTDs, however for our purposes, we will be focusing on the thin film platinum kind. Thin film refers to the style of the RTD element, or "sensing part;" platinum refers to the material of the RTD element. The specific RTDs used in CryoQ are purchased through Digi-Key [5]. They have $100\Omega \pm 0.06\%$ resistance and operate between $-200°C$ and $600°C$, with an accuracy of $\pm 15°C$ (see Figure 6).

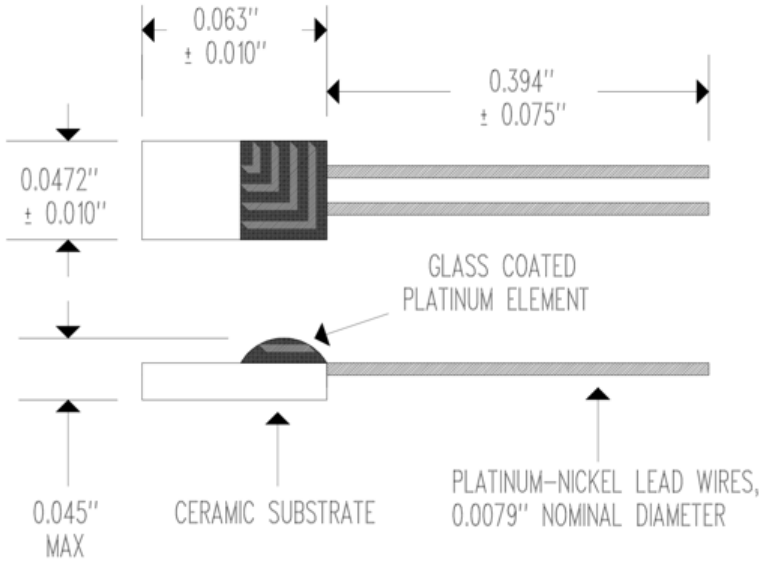

Figure 6: Detailed diagram of the resistance temperature detector currently in-use by the CryoQ experiment [16].

RTDs function by relying on the positive, nearly linear relationship between electrical resistance and temperature that is characteristic of metals. Platinum is considered an efficient choice because it is stable, nonreactive, and available in pure forms [15]. The relationship between electrical resistance and temperature is described by the Callendar-Van Dusen equation [17],

$$R_t = R_o(1 + At + Bt^2 + C(t - 100)t^3) \tag{1}$$

C is only applicable when $t < 0°C$
Let R_t = Resistance of the RTD at some temperature $t°C$ in Ω
Let R_o = Resistance of the RTD at $0°C$ in Ω

[5] https://www.digikey.com/products/en?keywords=615-1124-ND

A, B, and C are simply the coefficients determined by the type of RTD used, and they can be found using the following equations [18],

$$A = a + \frac{a\delta}{100} \tag{2}$$

$$B = \frac{-a\delta}{100^2} \tag{3}$$

$$C = \frac{-a\beta}{100^4} \tag{4}$$

Where a is the temperature coefficient of the material in $\Omega/\Omega/^\circ C$, typically a is $0.00392\Omega/\Omega/^\circ C$,

$$a = \frac{R_{100} - R_o}{100 + R_o} \tag{5}$$

δ is the second order term denoted by Callendar and represents the disparity between the actual temperature and the temperature calculated using only a, δ is typically 1.49 for pure platinum,

$$\delta = \frac{R_o[1 + a(260)] - R_{200}}{4.16 R_o a} \tag{6}$$

β is the fourth order term denoted by Van Dusen and represents the disparity between the actual temperature and the temperature calculated using only a and δ, typically $\beta = 0.1$,

$$\text{When } t > 0^\circ C, \beta = 0 \tag{7}$$

$$\text{When } t < 0^\circ C, \beta = \frac{t_l - [\frac{R_{t_l} - R_o}{R_o * a} + \delta(\frac{t_l}{100} - 1)(\frac{t_l}{100})]}{(\frac{t_l}{100} - 1)(\frac{t_l}{100})^3} \tag{8}$$

Let t_l be the low temperature end of the range

In physical terms, a small current is passed through the RTD. As the RTD experiences changes in temperature, its resistance changes values. This change is recorded by measuring the voltage across the RTD. Once the measurements have been made, the reading can be converted to temperature by applying a calibration equation specific to each RTD.

2.2.1. Sources of Error

There are three very common error sources, self-heating; resistor tolerance; and thermal offset voltages [19]. Due to the fact that current is being passed through the device, there is some heating contributed to the RTD. This will cause changes in the temperature. The self-heating error value is given by,

$$SH = I^2R * EK \tag{9}$$

Such that SH is the self-heating error
I is the current source
R is the resistance of the RTD at some temperature
EK is the self-heating coefficient in $\circ C/mW$

There are possible errors in the resistance of the device itself, a difference between expected resistance and the actual resistance. This error value is given by the resistor tolerance, and is often categorized into classes. There are four classes defined by the International Electrotechnical Commission standard (IEC 60751) [20],

Class C $= \pm(0.60 + 0.01 * t)$, for $(-50$ to $500C)$
Class B $= \pm(0.30 + 0.005 * t)$, for $(-50$ to $500C)$
Class A $= \pm(0.15 + 0.002 * t)$, for $(-30$ to $300C)$
Class AA $= \pm(0.10 + 0.0017 * t)$, for $(0$ to $150C)$
Where t is the temperature without regard to sign.

The classes inform you of the temperature deviation in degrees at any given temperature. Simply add the two terms, after the t has been accounted for and multiplied with the second term. For example, for class C at $t = 100$ or $-100°C$, the deviation is $\pm 1.6°C$. The thermal offset voltage, also known as the thermal electromotive force or Seebeck voltage, is produced at the joining of two different metals. It is due to the temperature difference between the two metals. The specific combination of metals give a temperature coefficient known as the Seebeck coefficient, with the unit μV/K.

2.2.2. Calibration

An essential part of getting an accurate temperature readout is dependent on how well-calibrated the device is, between the sensor input and the "real" temperature. Temperature calibration methods broadly fall into two categories, fixed-point and comparative. Fixed-point calibration is the more accurate of the two, although it is also more time-consuming and costly. This method works by testing at the fixed points of temperature at which a substance, such as nitrogen or gallium, experiences phase transitions. The intention is to choose points where the temperature readings can be consistently reproduced. The temperatures at these fixed points (triple, freezing, boiling) are defined by the International Temperature Scale of 1990 (ITS-90) [21]. The ITS is maintained by the National Institute of Standards and Technology (NIST). Calibration equipment include triple-point water cells ($900 to $2,000), calibration baths ($5,000 to $7,000), and dry-wells ($100 to $300). The NIST provides

laboratory calibration services, but costs can easily exceed $10,000 [22]. The platinum RTDs calibrated to NIST standards have a maximum expanded uncertainty of 0.54 mK, for the temperature range of 13.8033K to 273.16K. The coverage factor was not given in the reference material, but assumed to be k=2 [23].

Alternatively, comparative calibration is the more commonly used method. These tests are performed by comparing readouts from the RTD to a standard, laboratory-calibrated reference thermometer placed in the same environments. However, the Standard Platinum Resistance Thermometers (SPRT), with which we compare our uncalibrated RTDs, cost at least $1,000 [22]. In accordance to comparison calibration tests performed by NIST, there exists an expanded uncertainty (given k=2) of 2.3 mK for liquid nitrogen baths or 2.4 mK for ice and boiling water baths [24]. It is expected the we would receive similar results if NIST procedures are followed during our own calibrations. In performing any of these calibration tests ourselves, we would have to consider the consistency of procedures between the different detectors, the placement depth, the distance between detectors in the bath, and atmospheric pressure. Additionally, in order to be considered NIST traceable, the measurement equipment must eventually lead back to an NIST certificate.

Figure 7: The three resistance temperature detector probes, and a fourth tester probe, prepared for calibration baths by sealing in foil. One of the RTDs is attached in between two sample silicon disks. To ensure that the disk surfaces would not be scratched, I modified a plastic wafer container to accommodate for the wire. Once sealed in foil, they were inserted into plastic bags.

After going over the options, the first approach we took to calibrate our RTDs was to create our own calibration baths. We decided that having three fixed-points would be sufficient for an experimental temperature calibration curve. We planned to record the voltage readout of each RTD in a boiling water bath(373K), ice water bath (273K), and liquid nitrogen bath (77K). In doing so, we would be able to pair a voltage readout for each of those three temperatures, at which the respective phase transition occur. To begin,

I had to first prepare the RTDs for submersion. This is done as a precaution to protect the electrical components from water damage, and also to better our reading accuracy by enclosing the space versus leaving the RTDs in air. Initially, we tried puncturing a plastic container to house the RTDs and then sealing the opening with a varnish. However, this was not watertight and the varnish would not stick to the plastic. I was also concerned about the amount of material we were introducing between the sensor and the environment. I decided to enclose them in a resealable plastic bag instead. I started with the RTDs in room temperature, wrapped them individually in foil (the RTD mounted between two silicon disks was first placed in a case that I punctured to run the wires through) (see Figure 7), and placed all three RTDs in a plastic baggy that I checked was water-proof. The opening of the bag was sealed with Kapton tape. I checked that there weren't any strange or major changes in the readout, having placed the RTDs in the foil and baggy. There was also a spare RTD with leads that weren't soldered to a Lemo connector, I prepped that one the same way as a tester for the baths.

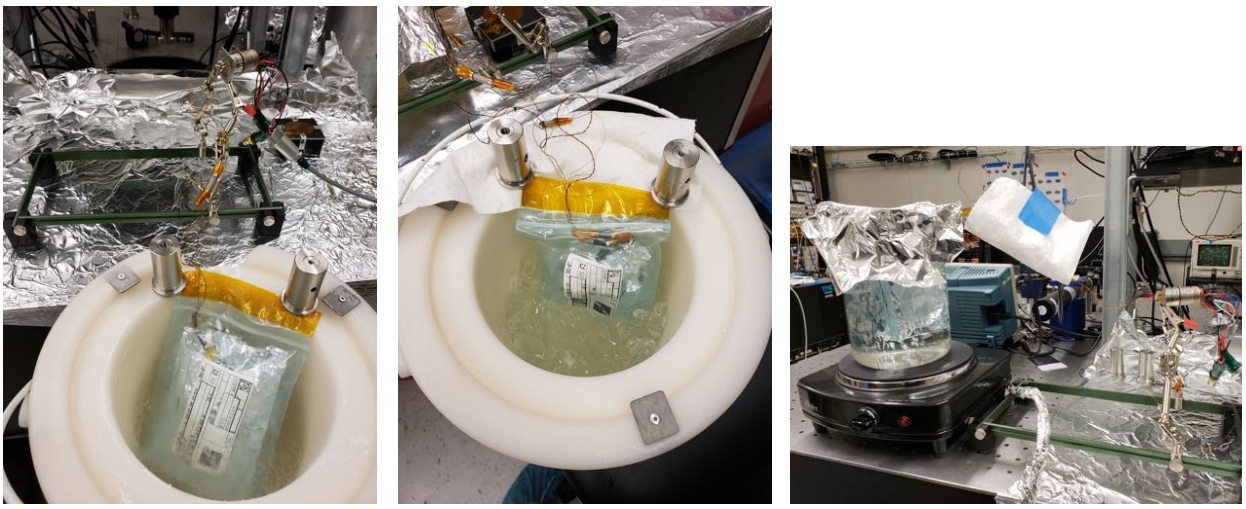

Figure 8: *Left:* Liquid nitrogen calibration bath at 77 K. *Middle:* Ice water calibration bath at 273 K. *Right:* Boiling water calibration bath at 373 K.

The first calibration bath to be used was liquid nitrogen (see Figure 8). I filled the Nalgene dewar with liquid nitrogen, and placed the tester RTD in for about 5 minutes to make sure there were no issues. Then the RTDs were put in around 1216932900 (GPS time). The dewar was covered, and the RTDs were left in the bath for about 10 minutes. For the second calibration bath, I filled the dewar completely with ice and filled in the space with water, keeping a high ice-to-water ratio (see Figure 8). While I let the mixture settle for about 10 minutes, I replaced the bag that was used in the nitrogen bath. After submerging the tester RTD for about 5 min, I placed the RTDs in around 1216071824 (GPS time). Again, the dewar was closed and the RTDs were left in for about 10 minutes. For the third calibration bath, I filled a 2000ml Pyrex beaker with water and placed it on a hot plate (see Figure 8). I covered the beaker with foil. After the water came to a boil, I placed the tester

RTD in for about 5 min. After checking that the tester RTD survived, I placed the RTDs in around 1216937100 (GPS time) and replaced the foil cover. The RTDs were taken out after about 10 minutes.

The calibration curves were created by taking an average of areas from the data where the voltage stabilized and stayed consistent after submersion. After pairing this with the respective temperature, as determined by the bath that was used, we were able to find the linear equation for each RTD's calibration curve. For RTD 1, the calibration curve in our desired temperature range can be described by the following equation, $y = 0.0082x + 0.1256$; for RTD 2, $y = 0.0092x - 0.0883$; and for RTD 3, $y = 0.0093x - 0.1472$ (see Figure 9). These values, considering the errors that may have been introduced during the calibration process, are just considered to be approximations. In an attempt for improved accuracy, we wanted to redo the calibration baths with the addition of a NIST-calibrated temperature diode in the same environment as the RTD. With this method, we can "correct" the RTD calibration curves according to the better trusted calibration of the NIST certified temperature diode. However, there were some difficulties in pairing the calibrated diode with the RTD circuitry. For sake of time, this method is to be reserved for future work instead, and the approximate values will be sufficient in the meantime.

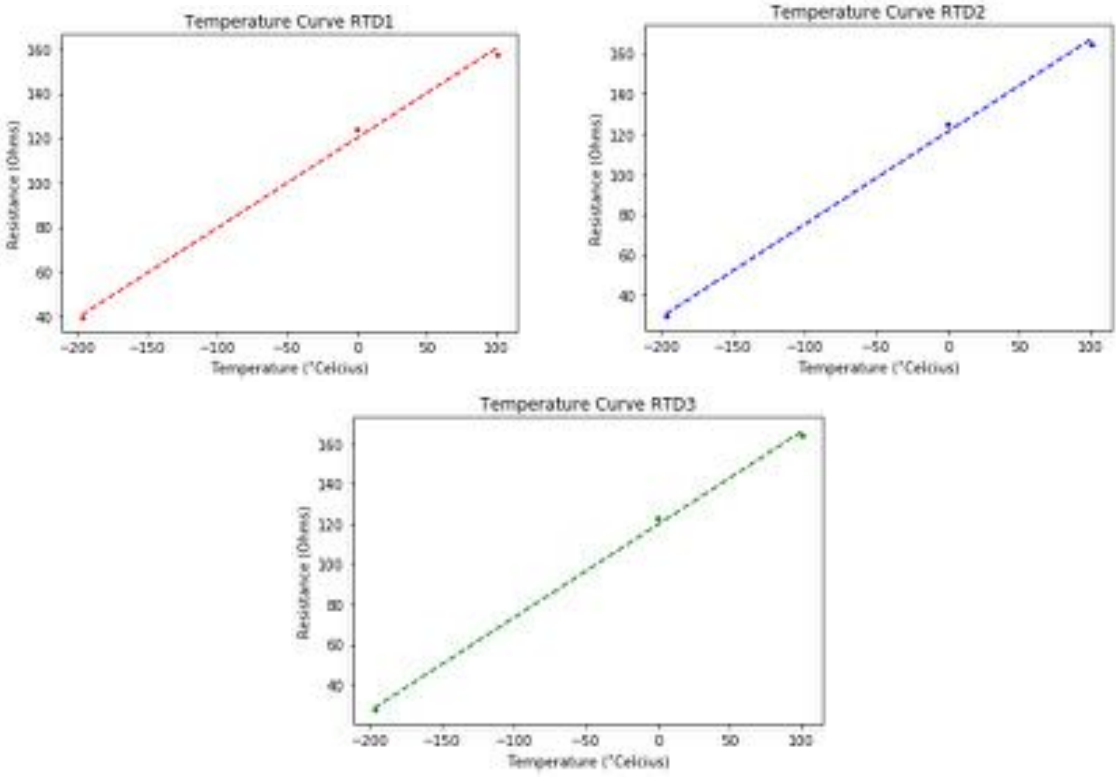

Figure 9: Graphs, in terms of temperature versus resistance, of the resulting calibration curves for each individual resistance temperature detector.

2.3. Beam Alignment

Once we acquired the temperature component of the calibration, we moved on to finding resonant frequencies to track. Before the CryoQ experiment can be used to make any measurements, the physical setup had to be prepared. A primary step was to align the laser beam (See Figure 10). The concluding arrangement placed the injection periscope close to the front of the disk, where the periscope will also capture the outgoing beam and direct it through the rest of the arrangement to the QPD.

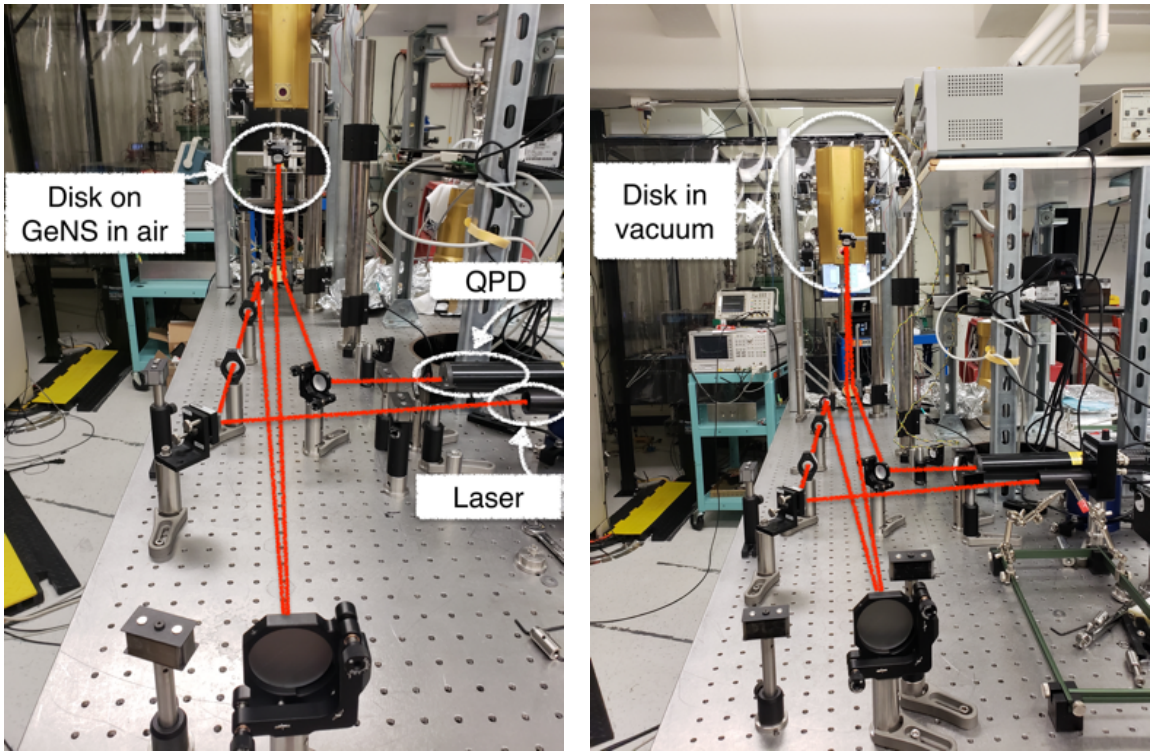

Figure 10: Two different, finalized versions of the laser optics layout, the path of the laser is highlighted in red for clarification. *Left:* The first layout we put together during the summer, in which GeNS suspends the disk on a platform outside of the cryostat. The laser makes its way through a beam splitter and periscope tower before reaching the disk. Once the laser is reflected off the disk, it makes it way back to the periscope, then off a few mirrors and through a series of telescoping lenses before reaching the QPD. *Right:* The second layout completed. After realization that the measurements were particularly difficult to make in-air, the disk was moved inside a cryostat to be contained in vacuum. GeNS suspends the disk within the cryostat. The laser optics were adjusted to account for the change.

2.4. The Ring-Down Method

The aforementioned method of measuring Q factor currently used by the CryoQ experiment is officially known as the ring-down method. The ring-down method works by exciting the material, then measuring the the amount of cycles it takes for the oscillation amplitude to halve. Within the CryoQ experiment, once the ring-down has begun, the activity is

recorded through the data acquisition system (DAQ). The data obtained in the time domain is then computed using a Fast Fourier Transform through the diagnostic GUI. The resulting power spectrum is then scanned for amplitude peaks that appeared due to the excitation.

During the summer, once we were able to obtain a few baseline measurements of the resonant frequencies at room temperature, I then continued by changing the temperature of the disk. The idea was to perform the entire experiment within a cryostat, however, an unresolved issue with one of the cryostat valves rendered it unavailable for cooling down. Due to the linear thermal response of the system, we were able to move forward with the project by sampling the disk at a raised temperature in place of cooling it down. The right-side picture in Figure 11 illustrates our first few attempts at performing the ring-down in air, with the disk heated using a heat lamp. As a result of being in air, environmental contributions led to unclear readouts for our initial trials. There, we moved the disk inside a cryostat to be used as a vacuum chamber, as depicted by the left-side picture in Figure 11.

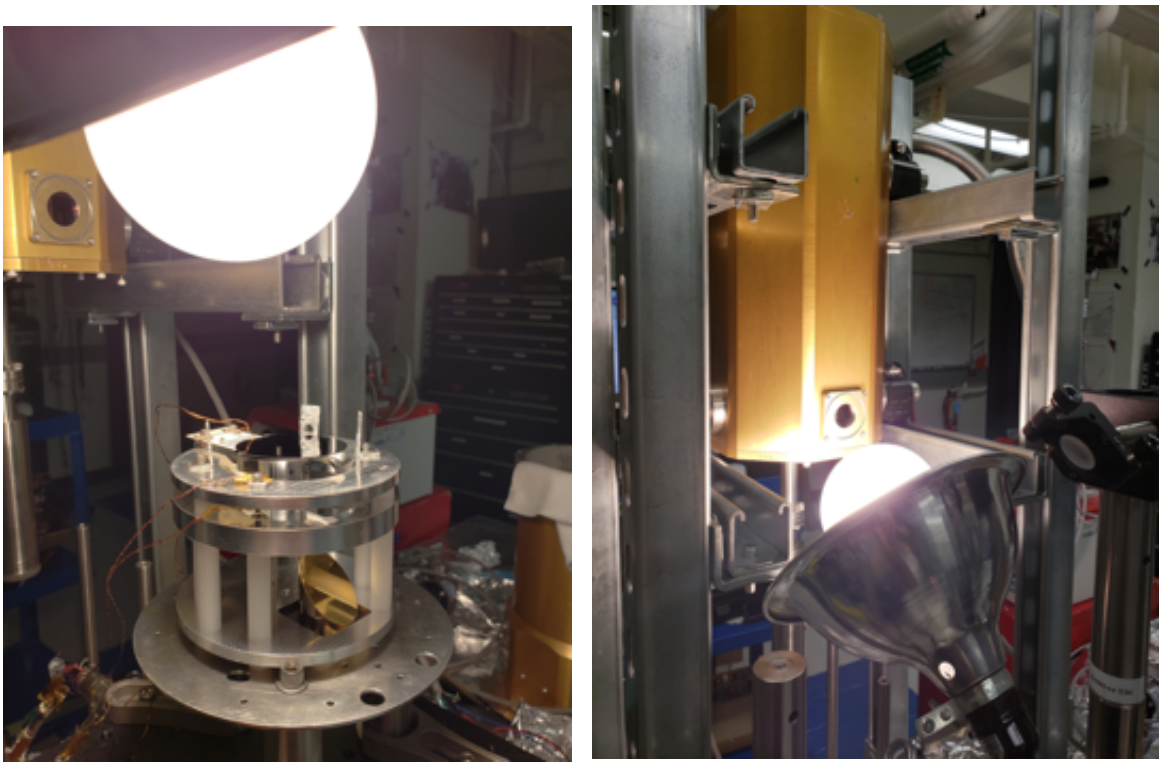

Figure 11: Close-ups of the heating process utilized to adjust the sample's temperature. *Left:* The first trial. *Right:* Second trial, the disk has been moved into the cryostat that was then pumped down.

3. Results

Using the RTDs to monitor the temperature of the disk and the ring-down method to monitor resonant frequencies, we were associate to a frequency shift with a shift in temperature. An example measurement is detailed through the graphs in Figures 12, 13, 14.

During this run, I began by recording the power spectrum of a disk without excitations and at room temperature (see Figure 12).

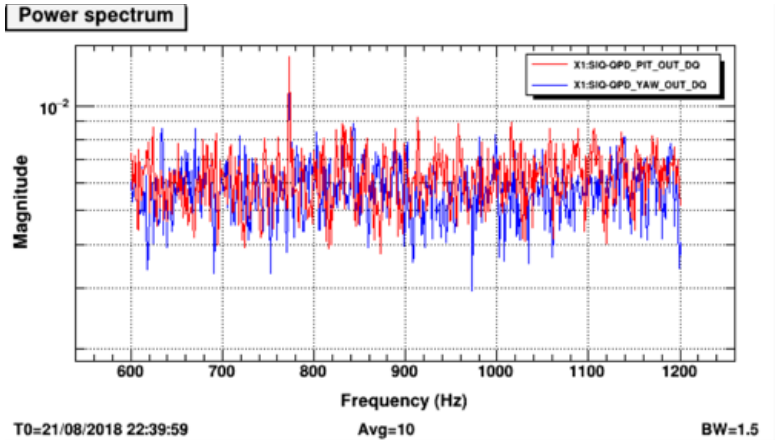

Figure 12: Power spectrum graph of Case 1, disk without excitations at room temperature, in-vacuum. The slight peak at around 775 Hz was noted as noise, occurring consistently throughout testing runs.

Then I continued by exciting the disk with white noise of range 100 to 3,000 Hz at room temperature. A resonant frequency at around 1008 Hz was found and tracked, I used this as our baseline measurement. By scanning for peaks, the highest amplitude was labeled at 1008.12 Hz (see Figure 13).

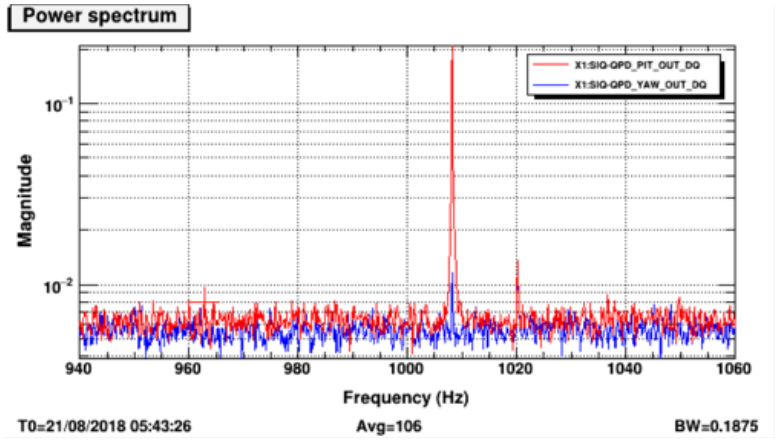

Figure 13: Power spectrum graph of Case 2, excited disk at room temperature, in-vacuum.

Utilizing the RTDs, we recorded that the disk started at a temperature of 300 K. After being heated with the heat lamp, this temperature rose to 310 K. After analyzing the power spectrum under these conditions, we found the high amplitude of the tracked resonant frequency to be 1007.88 Hz (see Figure 14). This means that there was a 240 mHz shift to the right in the resonant frequency. This led us to calculate the estimation that there is a 24 mHz shift in the resonant frequency for every unit of kelvin changed in this temperature range.

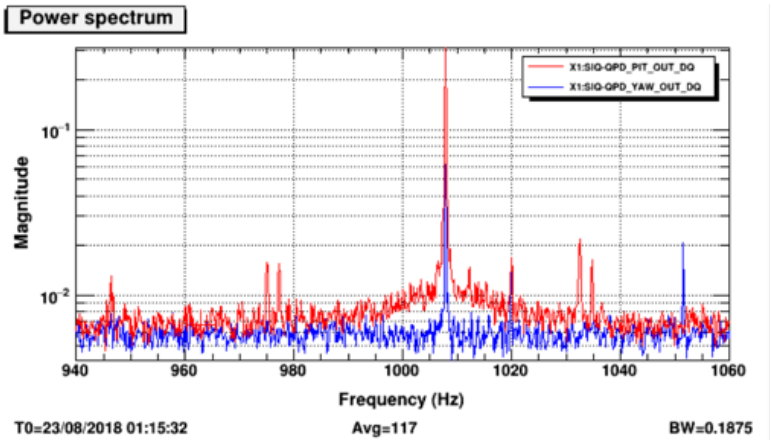

Figure 14: Power spectrum graph of Case 3, excited disk at 310 K, in-vacuum.

To verify the soundness of this calculation, we modified the following equation for the physical parameters of our own silicon sample [25],

$$\omega_1 = (1.875)^2 \frac{t}{L^2} \sqrt{\frac{E}{12\rho}} \tag{10}$$

Let t be the thickness of a homogenous silicon beam with a uniform cross section, L its length, E its Young's modulus, ρ its density. The beam's first eigenmode is given by,

For the silicon disk, given that E is the only parameter heavily dependent on temperature,

$$\omega \propto E \tag{11}$$

It follows then, that the eigenfrequency at some temperature T is,

$$\omega(T) = \frac{\omega_0}{\sqrt{E_0}} * \sqrt{E(T)} \tag{12}$$

We found that for this run, our theoretical resonant frequency should be at 1007.85 Hz. Compared to our actual frequency at 1007.88 Hz, this is an extremely close match and provides reassurance that our calculations are correct. For further conclusion, we must collect more data, preferably with the disk cooled to 123 K in the cryostat. Additionally, we should explore higher resonant frequencies for tracking.

4. Future Work

During this research project, we made progress by running several tests on the RTDs and providing a calibration curve for each probe. We were also able to align the laser beam and setup the physical components of the CryoQ experiment. Following that, we were able to track resonant frequencies and compare their shifts to temperature changes. To continue the effort, future work will need to be done with the RTDs and method of Q measurement. One of the first things to do will be pairing a laboratory-calibrated temperature diode with CryoQ's RTDs in order to perform a more accurate calibration. Additionally, an alternative Q measurement method known as ModeRinger can be utilized [26]. One primary reason that this method is an attractive alternative is because it will allow us to continuously manipulate parameters, such as temperature, at the same time the Q measurement is being made. This control will give us further insight on the temperature dependency of the sample. It will also be important to make more Q measurements, especially at colder temperatures, such as 123 K. Eventually, the current PID control loop should be modified to implement the real-time temperature monitoring given by the frequency and temperature shift calibration.

5. Acknowledgements

I would like to thank my wonderful mentors, Aaron Markowitz; Brittany Kamai; and Rana X. Adhikari, for providing patience and guidance that will prove inspirational beyond just the research lab. Additionally, thank you to Alan Weinstein, Julie Hiroto, Alex Urban, T.J. Massinger and everyone who supported the LIGO SURF students through this summer's lectures, accommodations, and events. Furthermore, for the encouragement, thank you to the LIGO SURF students and Dr. Brian Carter. Finally, for the incredible opportunity to work on a project that I am passionate about, I would like to thank the Laser Interferometer Gravitational Wave Observatory (LIGO), the LIGO Scientific Collaboration (LSC), the California Institute of Technology, the Student-Faculty Programs department, and their Summer Undergraduate Research Fellowship (SURF) program.

6. References

[1] A. I. Miller, A study of Henri Poincarés "Sur la Dynamique de l'Électron", Archive for History of Exact Sciences 10 (3-5) (1973) 207–328, URL https://www.researchgate.net/publication/237994124_A_Study_of_Henri_Poincare's_Sur_la_Dynamique_de_l'Electron.

[2] H. Poincaré, Sur la Dynamique de l'électron, Comptes Rendus de l'Academie des Sciences 104 (1905) 1504–1508.

[3] É. É. Flanagan, S. A. Hughes, The basics of gravitational wave theory, New Journal of Physics 7, ISSN 13672630, URL https://arxiv.org/abs/gr-qc/0501041v3.

[4] A. Einstein, A. Kox, M. J. Klein, R. Schulmann, On the General Theory of Relativity, vol. 6 of *Collected Papers of Albert Einstein*, Princeton University Press, 214–224, URL https://einsteinpapers.press.princeton.edu/vol6-doc/, 1996.

[5] R. V. Pound, G. A. Rebka, Gravitational Red-Shift in Nuclear Resonance, Phys. Rev. Lett. 3 (1959) 439–441, URL https://link.aps.org/doi/10.1103/PhysRevLett.3.439.

[6] R. A. Hulse, J. H. Taylor, Discovery of a pulsar in a binary system, The Astrophysical Journal 195 (1975) L51–L53, URL http://articles.adsabs.harvard.edu/cgi-bin/nph-iarticle_query?1975ApJ...195L..51H&data_type=PDF_HIGH&whole_paper=YES&type=PRINTER&filetype=.pdf.

[7] D. Walsh, R. F. Carswell, R. J. Weymann, 0957 561 A, B: twin quasistellar objects or gravitational lens?, Nature 279 (5712) (1979) 381–384, URL https://www.nature.com/articles/279381a0.

[8] B. P. Abbott, et al., Observation of Gravitational Waves from a Binary Black Hole Merger, Phys. Rev. Lett. 116 (2016) 61102, URL https://link.aps.org/doi/10.1103/PhysRevLett.116.061102.

[9] W. E. Althouse, S. D. Hand, L. K. Jones, A. Lazzarini, R. Weiss, Precision alignment of the LIGO 4 km arms using the dual-frequency differential global positioning system, Review of Scientific Instruments 72 (7) (2001) 3086–3094, URL https://doi.org/10.1063/1.1376138.

[10] E. Conover, L. Grossman, Trio wins physics Nobel for detecting gravity waves, URL https://www.sciencenewsforstudents.org/article/trio-wins-physics-nobel-detecting-gravity-waves, 2017.

[11] T. L. S. Collaboration, J. Aasi, B. P. Abbott, R. Abbott, et al., Advanced LIGO, Classical and Quantum Gravity 32 (7) (2015) 074001, URL http://stacks.iop.org/0264-9381/32/i=7/a=074001.

[12] D. V. Martynov, E. D. Hall, B. P. Abbott, et al., Sensitivity of the Advanced LIGO detectors at the beginning of gravitational wave astronomy, Phys. Rev. D 93 (2016) 112004, URL https://link.aps.org/doi/10.1103/PhysRevD.93.112004.

[13] L. S. Collaboration, Instrument Science White Paper URL https://dcc.ligo.org/T1600119/public.

[14] G. Vajente, A. Ananyeva, G. Billingsley, E. Gustafson, A. Heptonstall, E. Sanchez, C. Torrie, A high throughput instrument to measure mechanical losses in thin film coatings (April) (2017) 1–6.

[15] S. Kar, R. Sharma, Cryogenic Temperature Sensors, Defence Science Journal 57 (3) (2007) 195–208, URL http://citeseerx.ist.psu.edu/viewdoc/download?doi=10.1.1.865.9251&rep=rep1&type=pdf.

[16] PPG101A6 Product Information URL https://www.digikey.com/product-detail/en/us-sensor-littelfuse-inc/PPG101A6/615-1124-ND/3103189.

[17] WIKA, Callendar-Van Dusen equations for the calibration of platinum resistance thermometers URL https://www.wikapolska.pl/upload/DS_IN0029_en_co_59667.pdf.

[18] ITS, The Callendar – van Dusen coefficients URL http://www.itsirl.com/images/references/datasheets/1399021951CalVan.pdf.

[19] Keithley, Model 8681 Miniature RTD Surface Probe, Model 8681 Miniature RTD Surface Probe URL http://www.sophphx.caltech.edu/Lab_Equipment/RTD_temperature_probe.pdf.

[20] Omega, RTD Specifications URL https://www.omega.com/Temperature/pdf/RTDSpecs_Ref.pdf.

[21] Metrologia, The International Temperature Scale of 1990 URL https://www.omega.com/temperature/z/pdf/z186-193.pdf.

[22] NIST, NIST Calibration Program Calibration Services Users Guide SP 250 Appendix Fee Schedule – January 18 , 2018 URL https://www.nist.gov/sites/default/files/documents/2018/01/18/feeschedule2018.pdf.

[23] G. F. Strouse, W. L. Tew, Assessment of Uncertainties of Calibration of Resistance Thermometers at the National Institute of Standards and Technology URL https://www.nist.gov/sites/default/files/documents/calibrations/5319.pdf.

[24] G. F. Strouse, et al., A New NIST Automated Calibration System for Industrial-Grade Platinum Resistance Thermometers URL https://ws680.nist.gov/publication/get_pdf.cfm?pub_id=830609.

[25] U. Gysin, S. Rast, P. Ruff, E. Meyer, D. W. Lee, P. Vettiger, C. Gerber, Temperature dependence of the force sensitivity of silicon cantilevers, Phys. Rev. B 69 (2004) 045403, URL https://link.aps.org/doi/10.1103/PhysRevB.69.045403.

[26] N. D. Smith, A technique for continuous measurement of the quality factor of mechanical oscillators, Review of Scientific Instruments 86 (5) (2015) 053907, URL https://doi.org/10.1063/1.4920922.